International Journal of Fracture **116:** 179–194, 2002.

Exploration via electromagnetic radiation and fractographic methods of fracture properties induced by compression in glass-ceramic

D. BAHAT[1,*], V. FRID[1], A. RABINOVITCH[2] and V. PALCHIK[1]
[1]*The Deichmann Rock Mechanics Laboratory of the Negev and the Department of Geological and Environmental Sciences Ben-Gurion University of the Negev, Beer Sheva 84105, Israel*
[2]*The Deichmann Rock Mechanics Laboratory of the Negev and the Physics Department Ben-Gurion University of the Negev, Beer Sheva 84105, Israel*

Received 17 July 2001; accepted 11 June 2002

Abstract. The fracture properties of glass ceramic induced by compression were investigated by combined electromagnetic radiation (EMR) and fractographic methods. The study of a transparent sample enabled us to elucidate the sequence of crack nucleation, growth and interaction, and the ultimate longitudinal splitting under incremental increase of uniaxial stress in five stages. The fracture process was accompanied by some 18 EMR pulses. The short EMR pulses (of a duration of 0. 8–1.5 μs) occur under low stresses (0.36–1.7 MPa) in association with microcracking at the sample outer surface. Medium pulses (durations of 15–25 μs) are associated with stresses of up to 65 MPa and are correlated with crack limited growth outside the specimen. A lengthy pulse (duration of more than 40 μs) occurs under greater stresses (112 MPa) and correlates with the longitudinal splitting at failure. A return to the 17–20 μs range occurs for the post-failure cracking during stress relaxation.

Key words: Fracture, compression, electromagnetic radiation, fractography, glass- cramic, nucleation, longitudinal-splitting

1. Introduction

1.1. Electromagnetic radiation (EMR) induced in materials

This paper relates to the application of electromagnetic radiation (EMR) which is induced in materials when fractured. EMR was firstly observed by Stepanov (Urosovskaja, 1969) on fractured samples of sylvine (KCl) in 1933. This phenomenon was measured for fracture in various materials, including metals and alloys (Misra, 1975; Jagasivamani and Iyer, 1988), single crystals (Gold *et al.*, 1975; Khatiashvili,1984), rocks (Nitsan, 1977; Warwick *et al.*, 1982; Ogawa *et al.*, 1985; OKeefe and Thiel, 1995; Rabinovitch *et al.* 1995, 1996, 1998) and ice (Fifolt *et al.*, 1993; Petrenko, 1993). EMR is induced by mine rockburst (Khatiashvili, 1984; Frid, 1997a, b) and also appears as a precursor to earthquakes, some hours or even days before the earthquake event (King, 1983; Mogi 1985; Drakopoulos *et al.*, 1993; Johnston, 1991). Hence, EMR is associated with multi-scale fractures and is connected with various applications.

Several models on an atomic scale have been suggested to explain the EMR phenomenon. For example, it was considered that EMR is induced by the electric charges on opposite sides of elongated micro-defects (Nabarro, 1967; Finkel *et al.*, 1975), which might be due to the

*To whom correspondence should be addressed. E-mail: bahat@bgumail.bgu.ac.il

rupture of inter-atomic (ionic) bonds (Khatiashvili, 1984). It was also claimed that EMR was caused by breakdown when charge accumulation on two crack sides reached a limiting value (Gold, 1975; Finkel *et al.*, 1975; Cress *et al.*, 1987). However this conjecture was disproved in experiments, where EMR was associated with the movements of charged crack sides (Miroshnishenko and Kuksenko 1980; Gershenzon *et al.*, 1987). All these investigations were qualitative, and all efforts to use EMR for quantitative fracture prediction have not met with success, due to the lack of a detailed quantitative understanding of the EMR phenomenon (King, 1983; Rabinovitch *et al.* 1995, 1996).

In our previous work we showed that EMR appears as individual pulses or as pulse clusters (Rabinovitch *et al.*, 1995, 1996; Frid *et al.*, 1999). We have recently measured and parametrized individual EMR pulses and correlated them with crack dimensions (Rabinovitch *et al.*, 1998). In the present study we correlate specific EMR pulse parameters to specific cracks induced in glass-ceramic by uniaxial compression.

1.2. Fractography of transparent material

Fractography is the branch of science which analyzes fracture surface morphologies in technological materials and in rocks and determines the causes and mechanisms of failure (e. g. De Freminville, 1914; Bahat, 1991). We use a transparent material in the present study because, unlike our previous works, it enables us to characterize cracks that occur below the fracture surface and to determine the sequence of fracture events in the examined material. We experiment with a transparent glass-ceramic (Beall, 1989; Beall *et al.*, 1967) consisting of small crystals, not larger than the wavelength of visible light. Medium-sized and large crystals (> 0.1 mm) reduce the transparency of the material and the fractographic perfection of the fractured surface. The small size of the crystals in our specimen renders it to behave like glass.

2. Experimental

2.1. Sample shape and strength of experimental material

The resistance to failure of glass samples under uniaxial compression in compliance with standard specification dimensions (104 mm length and 52 mm in diameter) is greater than 450 MPa, which is beyond the load capacities of our press machine. Since our purpose was to overcome the resistance to fracture and to induce controlled cracking (rather than to investigate systematic strength properties) sample geometries deviating from standard specifications were tested. We obtained the best results on a truncated elliptic cone. Samples with elliptical cross section promise greater fracture intensities compared to samples with circular cross section (Bahat, 1991, p. 135; Bahat and Rabinovitch, 2000). Our sample length was 104 mm long, and the large and small diameters at the wide base end B were 33 mm and 21 mm, respectively, and the two diameters at the narrow top end of the truncated elliptic cone F, were respectively 33 mm and 10 mm (Figure 1).

2.2. Measurements

Our experimental system is described in detail in Rabinovitch *et al.*, (1998). It contains a stiff press machine ($5 \times$ GN/m stiffness), a magnetic 3 cm diameter loop antenna, very low noise electronics and an accurate oscilloscope connected to a computer (Figure 2).

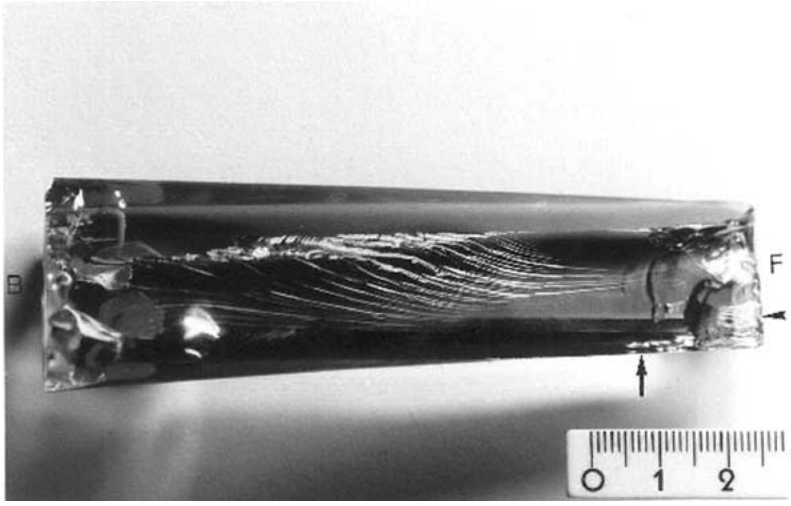

Figure 1. The main axial fracture of the large part of the sample at the end of the experiment (the termination of the fifth stage). B is the base of the truncated shaped sample and F is the end where the cone is cut off. The smooth section that appears dark is gradually transformed to the striae section. Horizontal arrow indicates position of the twisted-striae at the end of sample. Location of origin is approximately above vertical arrow (see text for explanation).

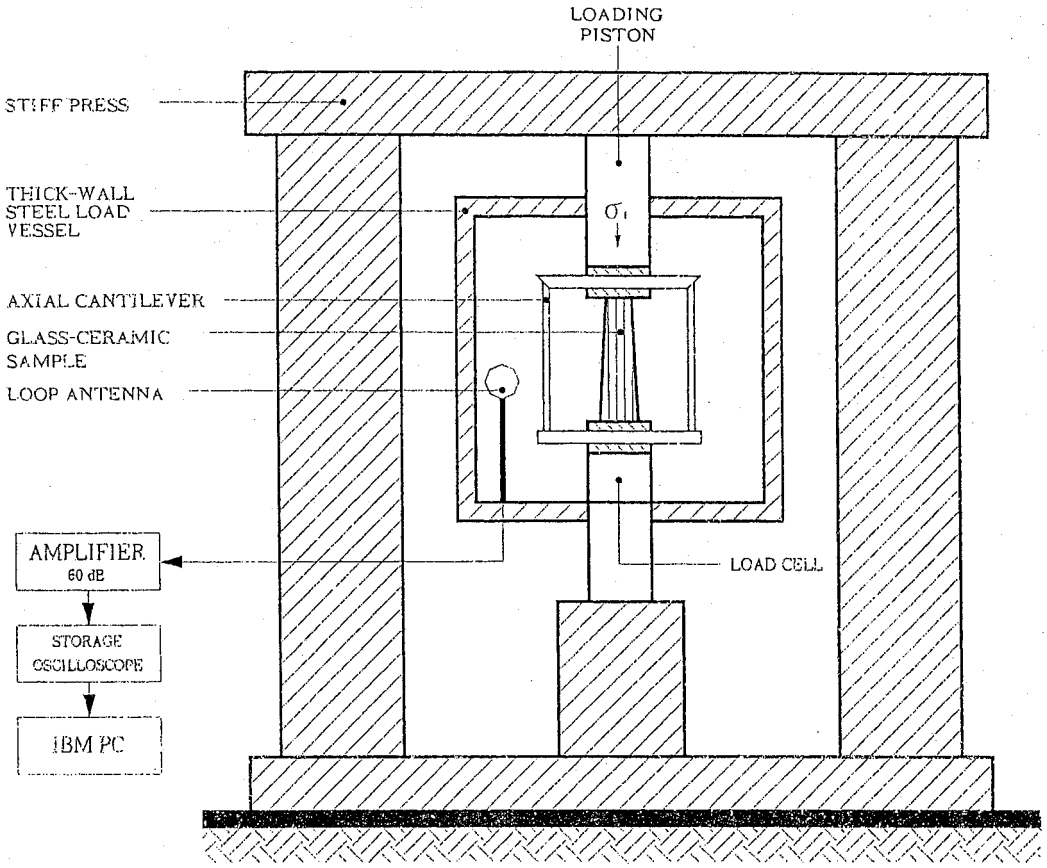

Figure 2. Schematic diagram of the experimental arrangement for monitoring simultaneously changes in stress, strain and electromagnetic radiation.

The load frame is combined with a closed-loop servocontrol (linearity 0.05%), which is used to maintain a constant axial piston rate of displacement. The load was measured with a sensitive load cell (LC-222M, maximum capacity 220 kN, linearity 0.5% full scale). The axial strain was measured by the axial cantilever (range about 10%; linearity 1% full scale). The antenna was situated 2 cm away from the center of the loaded samples with its normal vector pointing to the cone axis. We monitored EMR activity in the frequency band from 10 kHz up to 50 MHz with a sensitivity of 1 μV (microVolt) throughout. We loaded the sample with a strain rate of 5×10^{-6} s^{-1}. The press load was increased gradually and was stopped as soon as EMR was recorded. The sample was removed for a check and then the procedure started afresh. This procedure was repeated five times (denoted hereafter as five stages) (Figure 3).

3. Combined fracture and EMR results

Fractures occurred both at the outside surfaces of the sample (Figures 4 and 5) and along the 'main axial fracture' that divides the sample into two unequal elongated parts termed 'large' and 'small' (Figures 1 and 6). We first characterize the fracture properties of the sample and then correlate fracture parameters at the various stages of the experiment with the EMR parameters.

3.1. Five fracture stages under uniaxial compression

There is a considerable difference between the fracture patterns obtained at the smaller, F and the larger, B sample ends (Figure 1). Fracture was intense and occurred during the first four stages on the outer surface of the F end of the large part (Figures 4 and 5), but was only mild (one to three cracks) on the outer surface of B. However, the most intricate fracture process occurred during the fifth stage, revealing crack nucleation and axial splitting of the main axial fracture from top to bottom of the inside of the sample. Quite intriguing is the systematic evolution of the EMR signals throughout the five stages, matching well some of the EMR/fractographic correlations obtained from non-transparent materials (Rabinovitch *et al.*, 2000; Bahat *et al.*, 2001). The experimental results are summarized in Table 1.

3.2. The main axial fracture

Examination of the main fracture surface showed several important aspects of the fracture sequence, including: 1. The distinction between early cracks close to the sample tips and those in the nucleation zone at a remote location from the tips, 2. The continuous tensile surface of the longitudinal splitting, and, 3. The identification of post failure cracking. Different fracture events are identified on the surfaces of the two parts (the larger and the smaller one) that were formed by the longitudinal splitting.

3.2.1. *The main axial fracture of the large part*

The fracture surface of the large part is divided into three sections, which are: a. Cracking near the sample top F end (partly marked by the horizontal arrow in Figure 1); b. The striae section that stretches between F and B (Figure 1); and c. The smooth area with very delicate undulations (invisible in photo) in the dark section along the sample lateral edge, closest to the vertical arrow (Figure 1). We concentrate below on the striae in section b.

Striae cut the main fracture surface almost from end to end of the sample. They start from an origin that is located about 18 mm from the F end (see below) and 86 mm from the B end,

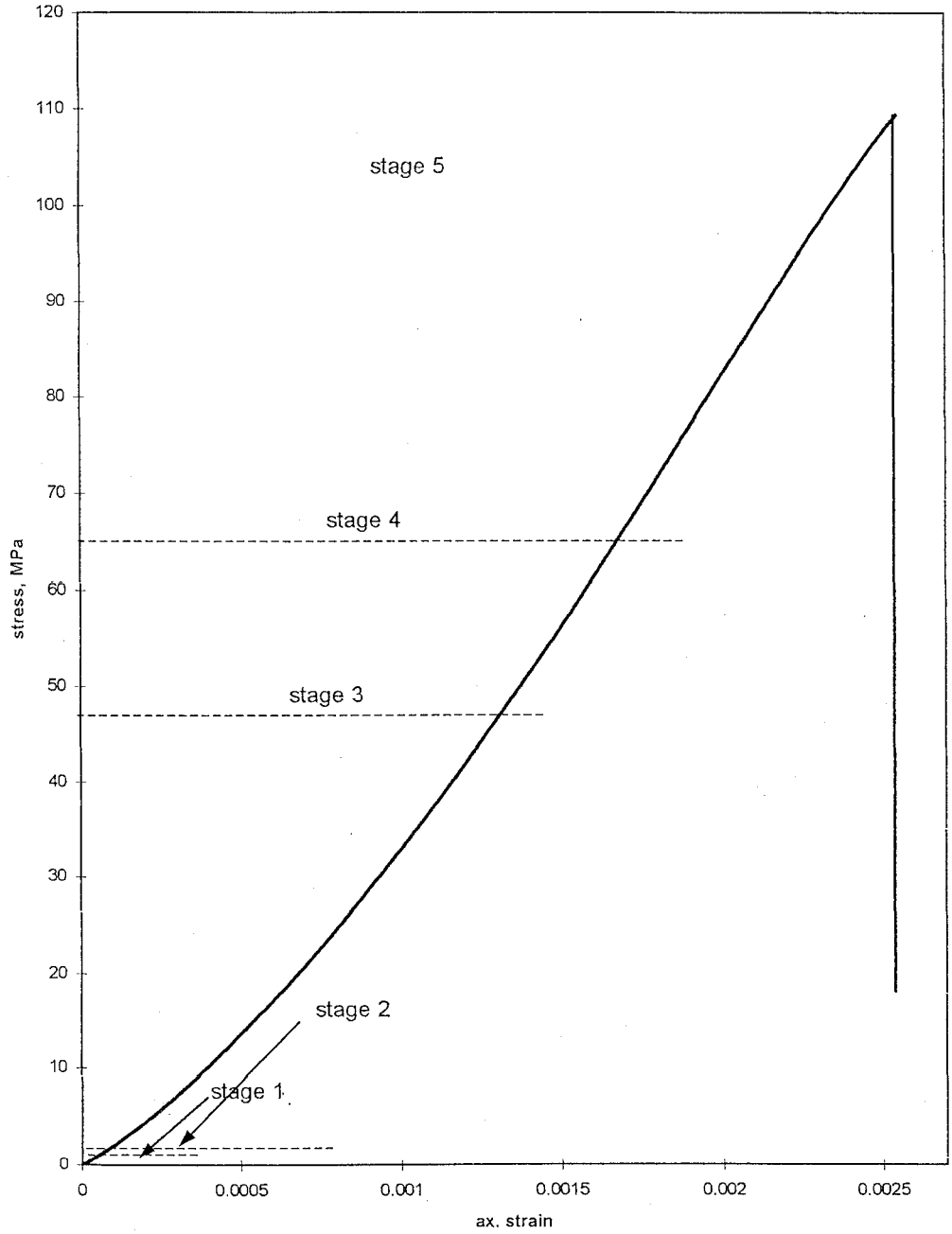

Figure 3. Stress versus strain for the fifth stage of the incremental stress increase. Dashed lines indicate stress levels achieved during stages 1–4.

Figure 4. Photograph of the outer surface of the F end of sample at the end of the experiment.

Table 1. EMR pulse parameters versus stress and strain in fractured glass-ceramic.

Stage	Stress MPa	Strain	Pulse number	Frequencies	T' μs	Pulse length	Crack size mm
1	0.36	0.00042	1	5.2, 27 (MHz)	0.95	Short	3.5 × 7.5
			2	5.7, 27 (MHz)	1.5	Short	
2	1.7	0.0011	1	1.2, 5.1, 18.4, 27.5 (MHz)	0.8	Short	2.0 × 7.0
			2	4.8, 19, 27 (MHz)	1.5	Short	3.5 × 10
3	47	0.0011	1	49.3, 156 (kHz)	25	Medium	2 × 5 × 19
4	0.9		1	46.7 (kHz)	15	Medium	10 × 10
			2	51.8 (kHz)	15	Medium	
	1.9		3	53, 85 (kHz)	25	Medium	
	3		4	41, 70, 122 (kHz)	17	Medium	
	5		5	72 (kHz)	20	Medium	
	12.5		6	100, 177 (kHz)	20	Medium	
			7	172 (kHz)	20	Medium	
	65	0.01850	8	172, 292, 468, 776 (kHz)	15	Medium	
			9	144, 225 (kHz)	15	Medium	
			10	75, 144, 225, 780 (kHz)	15	Medium	
5	112	0.025	1	18.7, 37.9 (kHz)	42	Lengthy	20 × 100
	$\ll$112		2	90 (kHz)	17	Medium	2.5 × 12
			3	40, 78, 242, 391 (kHz)	20	Medium	7 × 29

and is about mid distance (10 mm) from the two lateral edges of the main fracture (Figure 1). The striae radiate in two directions, towards the two ends of the specimen. The bulk of the striae propagated towards the B end, such that, with the increase of distance from the origin

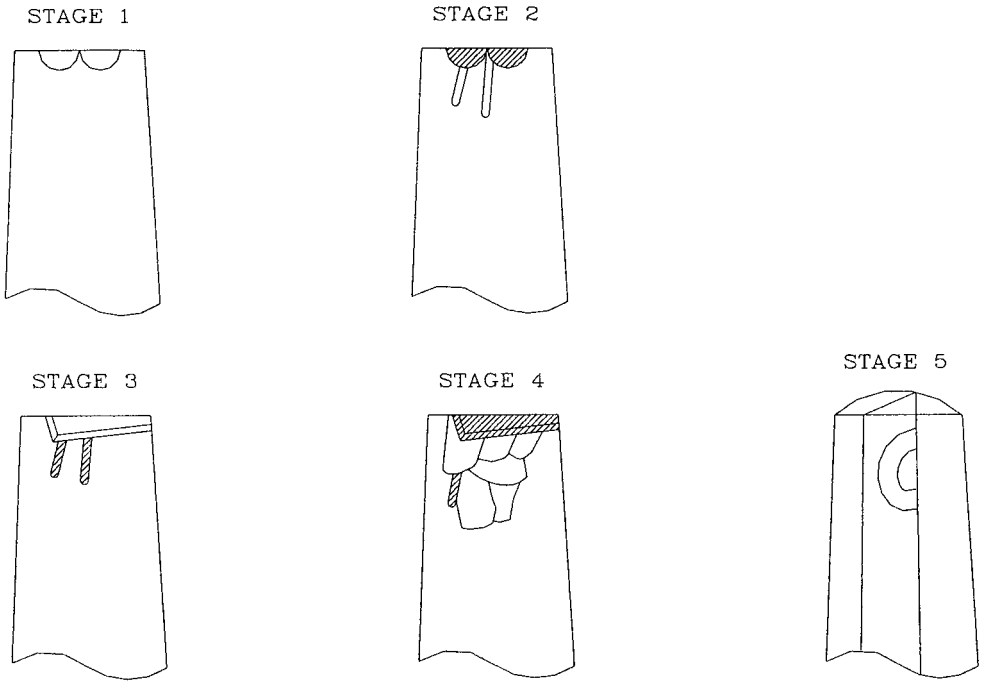

Figure 5. Diagramatic development of cracks at the outer surface of the F end of sample in five stages (see text for explanation).

gradual coarsening of the striae morphology occurs. Only three-four short (6–7 mm long) striae propagated towards the F end. Accordingly, the exact location of the origin, that is, the focus where the radial striae originated is within an area of 1–2 mm × 1–2 mm which we term the 'nucleation zone' (Figure 6a, inset). A microscopic examination indicates that the origin area is not associated with any morphological discontinuities (microcracks, kinked cracks, glass defects etc.), and the transparency of the sample enables us to verify that no microcracks occur underneath the origin. Various shades in axial and transversal-concentric orientations around the origin are reflections from the outer surface of sample and do not belong to the main fracture surface (Figure 6a).

3.2.2. *The main axial fracture of the small part*

The fracture surface of the small part is divided into four sections, which are:

a. Cracking near the sample top F end (closest to the scale in Figure 6b);

b. The Striae section (mostly emphasized at the opposite end from the scale);

c. The smooth section with very delicate undulations; and

d. This region cuts through the striae section and is divided into two cracks, I. the side-crack, and, II. the concentric-crack with coarse undulations (Figure 6b). The first three sections resemble their matching sections from the large part. We concentrate on section d.

Section d occurs exclusively on the small part. The 'side-crack' and the 'concentric-crack' differ considerably from each other. I. The side-crack is 12 mm long and 2. 5 mm wide. It started from the lateral edge of the sample some 10 mm away from the F tip and propagated steeply (bending between a dip of 20° to a dip of 40°) into the sample (Figure 6b).

II. The concentric crack has a semi-elliptical shape whose large and small diameters are 29 mm and 7 mm, respectively. It is shallow (dipping 5°–10°) and is enriched in concentric

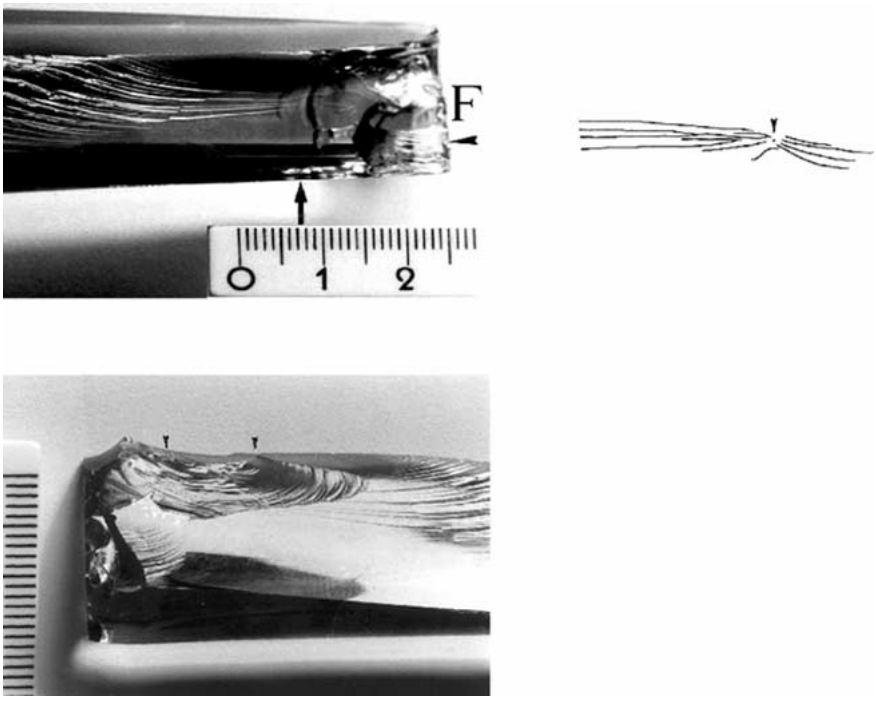

Figure 6. (a) An enlargement of the F end of sample from Figure 1, focusing on the nucleation zone above vertical arrow. While many (about nine) striae radiate from the origin towards the B end at left, fewer (some four) radiate towards the F end at right. Inset shows approximate origin location (the dot) at convergence of some twelve striae (see text for explanation). (b) The F end, showing the portion of the main fracture surface of the small part cut by the last two cracks from the fifth stage of experimentation. Two vertical arrows show the boundaries of the 'side-crack' along the lateral edge of sample.

undulations. The concentric-crack initiated from the end of the side-crack and propagated inside, partly cutting the main fracture surface at the striae region erasing the nucleation-site, and partly propagating underneath the main fracture without reaching the surface (invisible in Figure 6b).

3.3. Electromagnetic radiation and fracture parameters

3.3.1. *EMR parameters*

An EMR pulse (voltage A vs. time t, Figure 7) can be characterized by the following general relationship (Rabinovitch *et al.*, 1998):

$$A = \begin{cases} A_o \sin(\omega(t - t_o))(1 - \exp(-(t - t_o)/\tau)), & t < T \\ A_o \sin(\omega(t - t_o)) \exp(-(t - T)/\tau)(1 - \exp(-(T - t_o)/\tau)), & t \geqslant T \end{cases} \quad (1)$$

where t is the time, t_0 is the time from the origin up to the pulse beginning and T is the time from the origin up to the EMR pulse envelope maximum. Thus, $T' = T - t_0$ is the time interval to reach pulse envelope maximum, τ is the rise – and – fall times (RFT), which turn out to be the same, A_0 is the pulse amplitude and w is the frequency. We distinguish between three EMR pulse parameters, T', the frequency $f = \omega/(2\pi)$ and $T1$ (the time interval from pulse origin up to its fade out). We showed that the value of T' is determined by the crack length (Rabinovitch *et al.*, 1998). Note that $T1$ is a more complex parameter. It includes

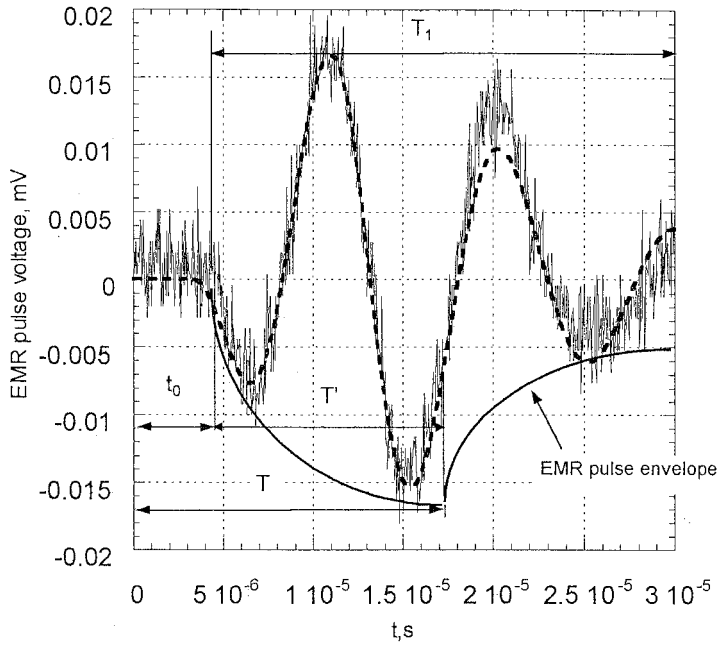

Figure 7. Characterization of an EMR pulse (voltage A vs. time t) (see text for explanation).

both T' and the pulse RFT. The RFT is determined by the decay processes in the material (heat, plastic deformation, etc.). The physical processes of the RFT origin are currently under investigation. Pulses with similar T' can have different RFTs and consequently different $T1$ values. Therefore, in this study we focus on T' and leave out $T1$. Stress and strain conditions, and EMR pulses were recorded in the five stages mentioned above (Table 1) and these were correlated with fracture characteristics.

3.3.2. *Correlation between EMR parameters and crack dimensions*

In our previous study (Rabinovitch *et al.*, 1998) we showed that T' was proportional to the number of broken chemical bonds and thus to crack length. In addition, based on general theory we asserted that the frequency was given by $f = V_R/2b$ where V_R was the Rayleigh velocity and b was the crack width (Rabinovitch *et al.*, 1998). These two assertions were supported by our previous experimental results (Rabinovitch *et al.*, 1999; 2000; Bahat *et al.*, 2001). In the present study we present direct correlations of these parameters by running the entire fracture process from crack nucleation to failure in a transparent material. For each individual (fractographically) visible crack we obtained four parameters: (1) crack length, (2) crack width, (3) EMR pulse T' and, (4) EMR pulse frequency. Characteristic pulses of different modes (Table 1) are represented in Figure 8.

Figure 9 shows an example of an EMR pulse of the fifth stage of loading with its least-square fit to Equation 1. As can be seen, both the accuracy of the measurement and that of the parametrization procedure are adequate ($R^2 = 0.96$). The results of parametrization of this EMR pulse ($T' = 42 \pm 0.3$ μs, $f = 18.7 \pm 0.012$ kHz,) are marked by arrows in Figures 10a,b.

We summarize the correlations between EMR T' and crack length, and between EMR frequency and crack width in Figures 10a and 10b, respectively. In both cases the points representing the stages from 3 to 5 fall well along the curve. Error bars on both graphs were

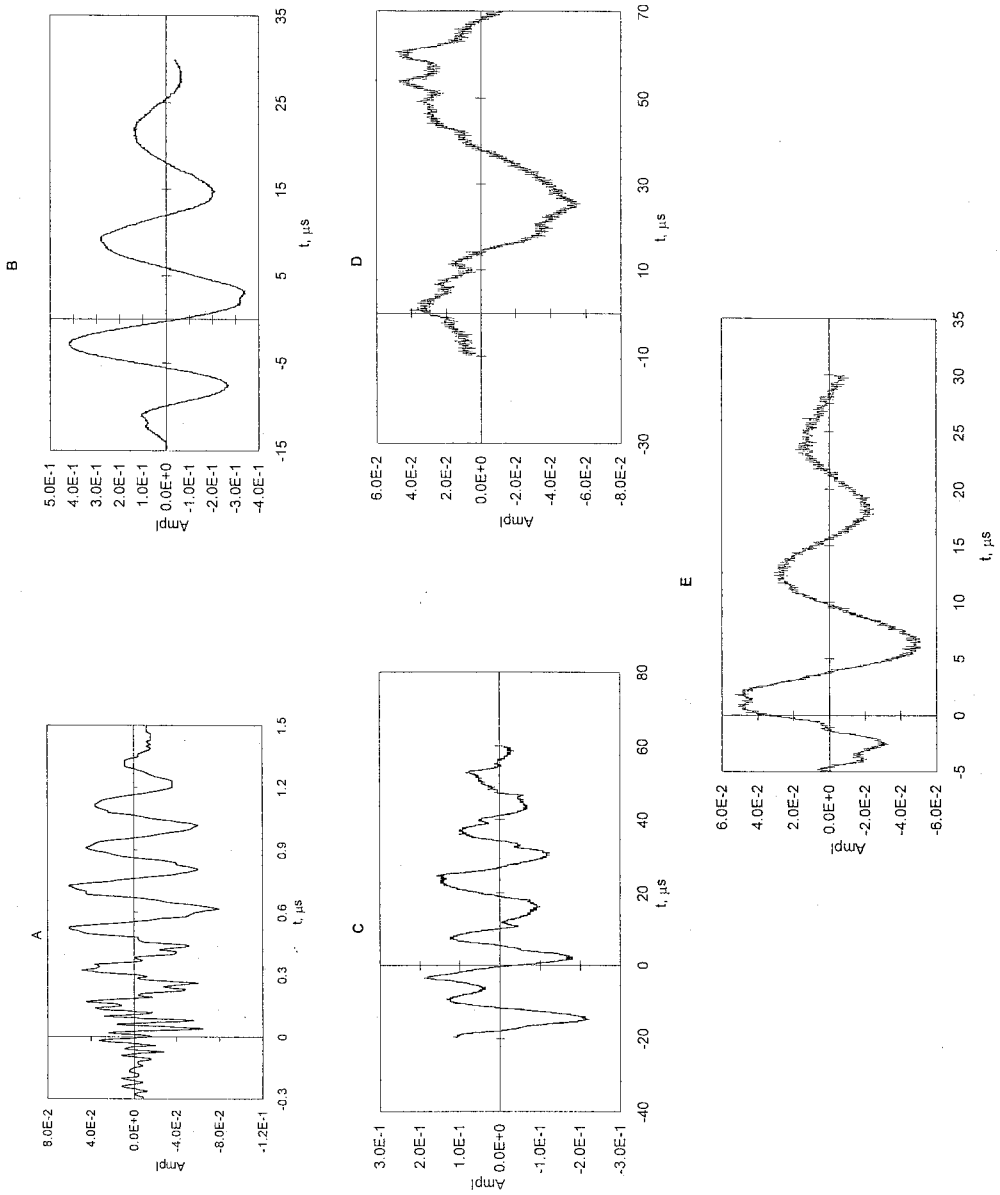

Figure 8. Characteristic pulses of the different modes (Table 1). (A) A short pulse (stage 1, pulse 1). (B) A medium, individual pulse (stage 4, pulse 7) (C) A medium, uneven pulse (stage 4, pulse 10). (D) A lengthy pulse (stage 5, pulse 1). (E) A medium, individual pulse (stage 5, pulse 2).

estimated by the spread of EMR data of the forth stage of loading, which were 3.5% for $\ln T'$ and 7.5% for $\ln \omega$.

The curve correlating T' to crack length shows a positive trend (Figure 10a). The dashed line indicates our assertion, $T' = 8.15 \times 10^{-7}$L where L is the crack length in mm and T' is in second. The R^2 coefficient obtained was 0.73. Considering the small number (five) of points, this coefficient is considered reasonable.

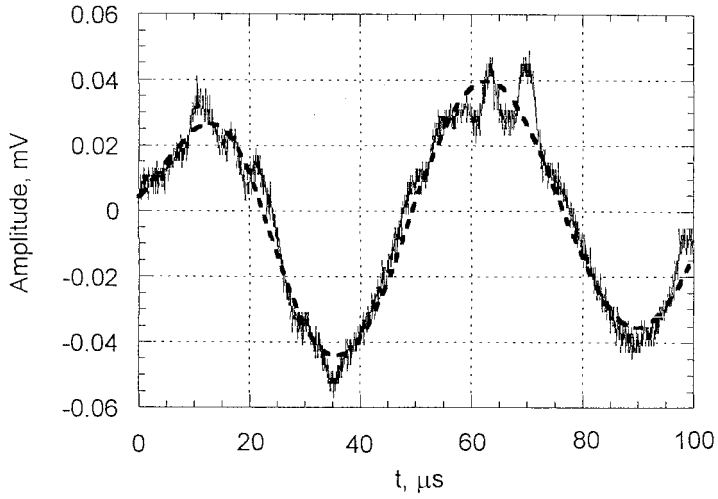

Figure 9. An example of an EMR pulse of the fifth stage with its least square fit to Equation 1 (dashed line). Results of fit: $T' = 42 \pm 0.3$ μs, $f = 18.7 \pm 0.012$ kHz, $R^2 = 0.96$.

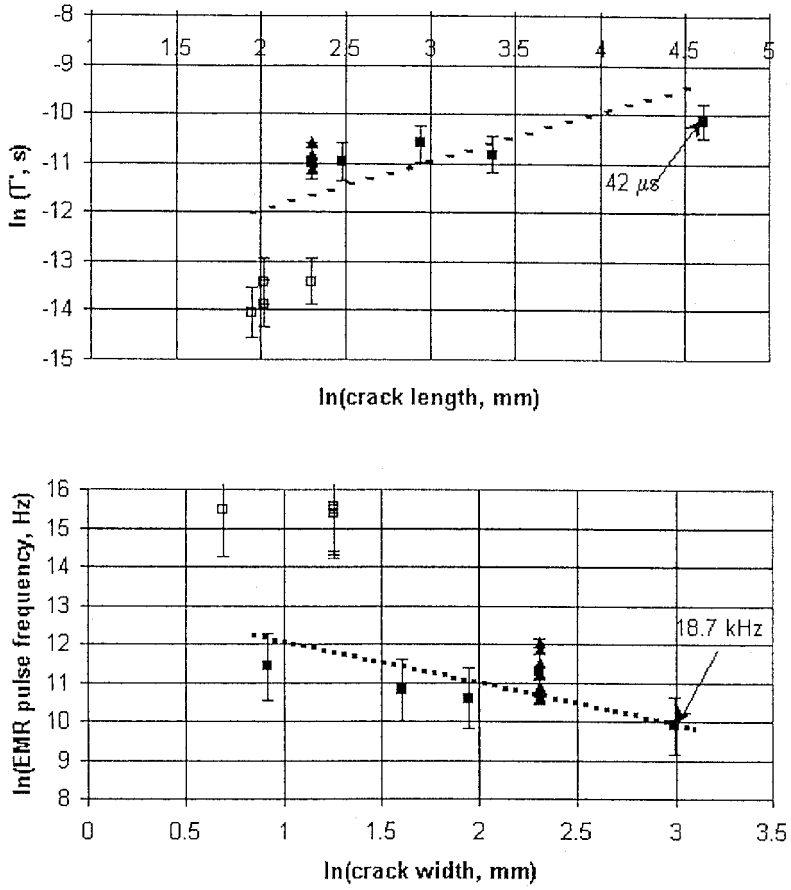

Figure 10. (a) Correlation between T' and crack length, and, (b) Correlation between EMR frequency and crack width. Open squares show EMR-fracture data during the first two stages, closed squares – stages 3–5; closed triangles show spread of EMR data during the forth stage. Error bars for both graphs were estimated by the spread of the EMR data of the forth stage of loading to be ~3.5% for $\ln T'$ and ~7.5% for $\ln \omega$.

The points in Figure 10b show a negative trend between f and b. The dashed line again, exhibits our assertion, which yields the relation $f = 413000/b$ (with R^2 of 0.78), where f is in Hertz and b is in mm. We estimate the theoretical crack velocity as follows: the measured Young modulus E and the density ρ of the glass-ceramics are 51.6 GPa and 2.37×10^3 kg/m^3, respectively. The Poisson ratio ν is assumed to be 0.25. Hence, the Rayleigh speed is $V_R = (0.87 + 1.12\nu/1 + \nu)\ (\mathrm{E}/2\rho(1+\nu))^{1/2} = 2704$ m/sec. The crack speed should be about 0.3 V_R (Sharon and Fineberg, 1999) or of the order of 1000 m/sec. A similar order of crack speed magnitude is obtained from the above relation of T.

4. Discussion

4.1. Early fracture at the outer surface

The dimensions of the flakes obtained by EMR parameters (about 0.3 mm in width and 1 mm in length) are much smaller than the measured flake dimensions (see Table 1). This discrepancy can be explained as follows. We assume that the initially created fractures during compression are in fact of small dimensions (as measured by the EMR). Eventually these fractures cause flaking off the external surface of the sample of much larger dimensions. The reason that the initial cracks were optically undetected stems from the fact that their apertures, which are not detected by EMR, were apparently below the wavelength of light.

4.2. Crack nucleation, longitudinal splitting and post-failure fracture

Pulses 8–10 from stage 4 developed at a considerably greater stress (65 MPa) than in stages 1–3 and in the early parts of stage 4 (Table 1). They generally exhibit fluctuating frequencies (172 kHz to 780 kHz, note particularly the latter) and a reduction in T' values (back to 15 μs). What are the implications of the changes that took place between pulses 7 and 8 of stage 4? Although visible early cracks clearly developed on the plane of the main axial fracture (near the F end in Figure 1), there is no direct observation which could place the exact time-stage and EMR properties associated with their formation. We however consider that these early cracks are correlated with pulses 8–10 of stage 4, for the following reasons:

1. The significant increase in stress (from 12.5 to 65 MPa) before the development of the main axial fracture (which developed at stage 5) indicates a drastic change in fracture conditions, which in turn suggests a new fracture mode. The latter could be manifested by micro cracking in a location which had not already cracked, initiating the inside plane of the main axial fracture (not on the outside of the sample).
2. The reverse trend in T' from a gradual increase to a decrease also indicates an important change in fracture conditions. Particularly, the reduction in T' suggests the formation of smaller cracks compared to the earlier ones of stage 4.
3. Finally, the high pulse frequencies, particularly the last ones of pulses 8 and 10 (776 kHz and 780 kHz, respectively) which approach the frequencies of the initial cracks of stages 1 and 2 also reflect probable microcracking. This information provides a general idea about the possible EMR properties which are correlated with the crack development which is a precursor to the growth process of the longitudinal axial splitting.

Two previous investigations of failure by uniaxial compression resulted in different observations. Holzhausen and Johnson (1979) argue that generally, with no buckling, longitudinal splitting cannot occur by tension parallel to the specimen axis. If however, buckling of the rock

occurs, splitting may be initiated within the sample, and may propagate axially by tension to both ends of the cylinder. Nemat-Nasser and Horii (1982) on the other hand, suggest that relative frictional sliding of the faces of pre-existing cracks at various angles that deviate from axiality may produce at their tips tension cracks that curve into 'wing cracks' and grow stably parallel to σ_1. The overall smoothness of the longitudinal split (all along section c) suggests that fracture growth did not occur by a mechanism of interacting groups of wing cracks, that would lead to some roughness on the fracture surface. The implication is that fracture nucleation and growth were tensile and continuous. In addition, the straight planar shape of the longitudinal split does not show any evidence of buckling. Therefore, if buckling occurred it must have been elastic.

Stage 5 is divided into two parts. First, the propagation of the main axial fracture (first pulse of stage 5, Table 1) that occurred at very high stress (112 MPa) and with a very high T' (42 μs). Second, the additional two pulses which appeared at much lower T' values. The first of the two (pulse 2, stage 5) consisted of a single frequency, whereas the second one (pulse 3) consisted of four frequencies. This distinction corresponds quite well to the fractographic observation, which distinguishes two cracks that developed in sequence, the second of which cut the main axial fracture. The crack associated with pulse 2 (between two arrows in Figure 6b) is fairly uniform whereas the crack which is correlated with pulse 3 (the shallower and longer crack in Figure 6b) is subdivided into a series of many concentric undulations. This constitutes an experimental proof of two post failure cracks that developed during stress relaxation from its maximum. Note that no EMR pulses and no cracks were registered during unloading and restarting in stages 1–4 and in the restarting of stage 5.

4.3. Comparison between fracture in strong glass-ceramic and weak chalk

The fracture pattern of the glass-ceramic is significantly different from that obtained in chalk by similar (uniaxial) experimental conditions (Bahat *et al.*, 2001). Chalk samples failed by multi-fractures into numerous parts (up to 18 pieces larger than 100 mm^2), reflecting many independent fracture origins, rather than a single nucleation zone that leads through a single split to only two parts. This difference may be linked to the relatively low strength of chalk (which is lower than 53 MPa) compared to glass-ceramic (that is more than twice stronger, Table 1). In addition, the glass ceramic behaved as a uniform material whereas the porous chalk revealed non-uniform fracture surfaces (Bahat *et al.*, 2001). Hence, the weaker and porous material promoted heterogeneous fracture behavior (Jaeger and Cook, 1979) resulting in the creation of many crack nucleation centers, compared to the relative homogeneity in the stronger and non-porous material that caused failure to initiate from a single nucleation site.

4.4. Verification of previous results

In our previous studies we implicitly showed that crack length is directly proportional to T' and crack width is inversely proportional to ω. Here these relations were demonstrated by direct correlation between measured crack dimensions and EMR parameters (Table 1).

5. Summary

We applied uniaxial compression on transparent glass ceramic by an incremental test in five stages, and observed the fracture process from nucleation through failure by longitudinal splitting up to post-failure fracture during stress relaxation.

A fracture origin was located at about the centre of a nucleation zone on the plane of the longitudinal splitting and was recognized at the focus by bilateral striae. The nucleation zone developed within the material at a distance of about 10 mm from one tip of the sample.

The planar shape of the longitudinal split and its overall continuation and smoothness suggest that both fracture nucleation and fracture growth were tensile and continuous.

The fracture process was accompanied by some 18 EMR pulses.

Correlation of T' (the time interval to reach pulse maximum) with the mechanical parameters reveals that short pulses (of a duration of 0.8–1.5 μs) occur under low stresses (0.36–1.7 MPa) in association with microcracking at the sample outer surface. Medium pulses (durations of 15–25 μs) are associated with stresses of up to 65 MPa and are correlated with crack limited growth outside the specimen. At the nucleation zone T' stayed constant at 15 μs for the cracks . A lengthy pulse (duration of more than 40 μs) occurred under greater stresses (112 MPa) and is correlated with the longitudinal splitting at failure. T' returned to the range 17–20 μs for the post-failure cracking that occurred under stress relaxation.

The present investigation combines for the first time experimentation by uniaxial compression and fractographic methods in analyzing EMR induced by fracture in glass-ceramic. Whereas in previous studies we interpreted correlations between EMR parameters and crack dimensions only indirectly, the present study confirms these correlations directly.

Compared to fracture in a weak and porous material (chalk) that resulted in some 18 pieces due to many crack nucleation sites, the present failure initiated from a single nucleation zone forming only two pieces.

Acknowledgements

George H. Beall from Corning Incorporated, Corning N. Y. most kindly provided us with glass-ceramic samples for experimentation. We would like to thank the Israel Science Foundation founded by the Israel Academy of Sciences and Humanities for supporting this study (research No. 244/99-2).

References

Bahat, D. *Tectonofractography*, Springer-Verlag (1991) 354 pp.

Bahat, D., Rabinovitch, A. and Frid, V. Fracture characterization of chalk in uniaxial and triaxial tests by rock mechanics, fractographic and electromagnetic radiation (EMR) methods. *Journal of Structural Geology* **23** (2001) 1531–1547.

Cress G.O., Brady B.T. and Rowell G.A. Sources of electromagnetiuc radiation from fracture of rock samples in the laboratory. *Geophysical Research Letters* **14** (1987) 331–334.

Beall, G.H. Design of glass-ceramics. *Reviews of Solid State Science* **3** (1989) 333–354.

Beall, G.H. Karstetter, B.R. and Rittler, H.L. Crystallization and chemical strengthening of stuffed βtquartz glass-ceramics. *J. Amer. Ceram. Soc.* **50** (1967) 99–108.

De Freminville M. Ch. Recherches sur la fragilite – l'eclatement. *Rev. Met*. **11** (1914) 971–1056.

Drakopoulos J., Stavrakakis, G.N., and Latoussakis, J. Evoluation and interpriration of thirteen official vantelegrams for the period september 10, 1986 to april 28, 1988. *Tectonophysics* **224** (1993) 223–236.

Fifolt D. A., Petrenko, V.F. and Schulson, E.M. Preliminary study of electromagnetic emissions from cracks in ice, *Philosophical Magazine B* **67**(3) (1993) 289–299.

Finkel V.M. Golovin Y.I. and Mogila, P.G. Electrical effects accompanying fracture of LIF crystals and problem of crack control. *Soviet Physics-Solid State* **17**(3) (1993) 492–495.

Frid V. Electromagnetic radiation method for rock and gas outburst forecast. *Jounal of Applied Geophysics* **38** (1997a) 97–104.

Frid V. Rock-burst hazard forecast by electromagnetic radiation excited by rock fracture. *Journal of Rock Mechanics and Rock Engineering* **30** (4) (1997b) 229–236.

Frid, V., Bahat, D., Goldbaum, J. and Rabinovitch, A. Potential geophysical applications of electromagnetic radiation induced by rock fracture: experimental and theoretical. *Israel Journal of Earth Sciences* **49** (2000) 9–19.

Gershenzon N., Zilpimiani D. and Manguladze, P. Electromagnetic radiation from tip of crack during ionic crystal fracture, *Doklady Akademii Nauk SSSR* **288** (1985) 75–84.

Gershenzon N., Gokhberg, M. and Morgunov, V. Sources of electromagnetic emission presiding seismic events. *Physics of the Solid Earth* **23** (2) (1987) 96–101.

Gokhberg M., Yoshino, T. and Morgunov, V. Results of recording operative electromagnetic earthquake precursor in Japan. *Physics of the Solid Earth* **18**(2) (1982) 144–146.

Gokhberg M., Gufel'd, I. and Gershenzon, N. Electromagnetic effects during rupture of the Earth Crust, *Physics of the Solid Earth* **21** (1985) 52–63.

Gold R.M., Markov G. and Mogila P.G. Pulsed electromagnetic radiation of minerals and rocks subjected to mechanical loading. *Physics of the Solid Earth* **7** (1975) 109–111.

Holzhausen, G.R. and Johnson, A.M. Analyses of longitudinal splitting of uniaxially compressed rock cylinders. *International Journal of Rock Mechanics and Mining Sciences & Geomechanics Abstracts* **16** (1979) 163–177.

Jagasivamani, V. and Iyer, K.J.L. Electromagnetic emission during fracture of heat-treated spring steel, *Materials Letters* **6**(11–12) (1988) 418–422.

Jaeger, J.C., and Cook, N.G.W. *Fundamentals of rock mechanics*, Chapman and Hall, London (1979) 593 pp.

Johnston, A.C. Light from seismic waves. *Nature 3* **53** (1991) 610.

Khatiashvili, N. The electromagnetic effect accompanying the fracturing of alkaline halide crystals and rocks. *Physics of the Solid Earth* **20** (1984) 656–661.

King, C.Y. Electromagnetic emission before earthquake. *Nature* **301** (1983) 377.

Miroshnichenko, M. and Kuksenko, V. Study of electromagnetic pulses in initiation of cracks in solid dielectrics *Soviet Physics-Solid State* **22**(5) (1980) 895–896.

Misra, A. Electromagnetic effects at metallic fracture. Nature **254** (1975) 133–134.

Mogi, K. *Earthquake prediction.* Academic press, Tokyo, (1985) 382 pp.

Nemat-Nasser, S. and Horii, H. Compression-induced nonplanar crack extension with application to splitting, exfoliation, and rockburst. *Journal of Geophysical Research* **87** (1982) 6805–6821.

Nesbitt, A.C. and Austin, B.A. The emission and propagation of electromagnetic energy from stressed quartzite rock underground. *The Trans. of the SA Inst. of Electr. Eng.* **79** (1988) 53–56.

Nabarro, B. *Theory of crystal dislocations*, Oxford University Press, (1967) 821 pp.

Nitsan, V. Electromagnetic emission accompanying fracture of quartz-bearing rocks. *Geophysical Research Letters* **4**(8) (1977) 333–336.

OKeefe, S.G. and Thiel, D.V.A mechanism for the production of electromagnetic radiation during fracture of brittle materials, *Physics of Earth and Planetary Interior* **89** (1995) 127–135.

Ogawa, T., Oike, K. and Miura, T. Electromagnetic radiation from rocks. *Journal of Geophysical Research* **90** (d4) (1985) 6245–6249.

Rabinovitch, A., Bahat D. and Frid, V. Comparison of electromagnetic radiation and acoustic emission in granite fracturing. *International Journal of Fracture* **71**(2) (1995) r33–r41.

Rabinovitch, A., Bahat, D. and Frid, V. Emission of electromagnetic radiation by rock fracturing. *Z. Geol. Wiss.* **24**(3–4) (1996) 361–368.

Rabinovitch, A., Frid, V. and Bahat, D. Parametrization of Electromagnetic radiation pulses obtained by triaxial fracture in granite samples. *Philosophical Magazine Letters* **77** (1998) 289–293.

Rabinovitch, A., Frid, V., Bahat D. and Goldbaum, J. Fracture area calculation from electromagnetic radiation and its use in chalk failure analysis. *International Journal of Rock Mechanics and Mining Sciences*. **37** (2000) 1149–1154.

Urusovskaja A.A. Electric defects associated with plastic deformation of ionic crystals. *Soviet Physics – Uspekhi* **11** (1969) 631–643.

Warwick J.W., Stoker C. and Meyer T.R. Radio emission associated with rock failure: possible application to the great Chilean earthquake of May 22, 1960) *Journal of Geophysical Research* **87**(b4) (1982) 2851–2859.